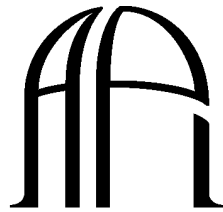# Millimeter-wave scattering polarization from vertically stratified protoplanetary disks

ANTON PANNEKOEK
INSTITUUT

A bachelor thesis presented by the
Anton Pannekoek Institute

Nick van Santen

Daily supervisor : Dr. Ryo Tazaki
First examiner : Prof. Dr. Carsten Dominik
Second examiner : Prof. Dr. Alex de Koter

22 July 2021

VU VRIJE UNIVERSITEIT AMSTERDAM | UNIVERSITEIT VAN AMSTERDAM

Nederlandse Samenvatting

Planeten ontstaan uit kleine gas en stofdeeltjes die zich samen klonteren om steeds groter en groter te worden. Dit gebeurt in een zogeheten protoplanetaire schijf. Deze schijf bestaat uit al deze kleine gas en stofdeeltjes waar uiteindelijk planeten uit ontstaan. In het begin zijn deze deeltjes rond de 1 micrometer groot, een duizendste millimeter. Wanneer deze deeltjes tegen elkaar aan botsen dan blijven ze aan elkaar vast plakken. Door middel van dit mechanisme groeien de deeltjes. Op een gegeven moment worden de deeltjes echter te groot en energiek. Nu stuiteren de deeltjes van elkaar af of verpulveren ze elkaar. Wanneer dit gebeurt, dan hebben de deeltjes de groei-barrière bereikt. Momenteel is nog onduidelijk bij welke grote van de deeltjes nou precies de groei-barrière is bereikt.

Er zijn twee methoden om te bepalen hoe groot de deeltjes zijn. De eerste methode is het meten van de intensiteit van de protoplanetaire schijf. Dit wordt daarna vergeleken met berekeningen die zijn gedaan voor verschillende type en grootte deeltjes. Hieruit kon men concluderen dat deeltjes bij de groei-barrière millimeter of groter moeten zijn.

De tweede methode is om naar de polarisatie van het licht te kijken dat afkomstig is van de protoplanetaire schijf. De polarisatie van licht geeft aan in welke "richting" het licht staat. Onderzoekers hebben toen deze resultaten proberen te repliceren door middel van een model van de protoplanetaire schijf. Dit model kon de gevonden polarisatie repliceren met deeltjes die ongeveer 100 micrometer groot zijn.

Deze twee methoden spreken elkaar dus tegen. De eerste methode bepaalde, aan de hand van de intensiteit, dat de deeltjes millimeter of groter zijn, terwijl de tweede methode, met behulp van de polarisatie, bepaalde dat de deeltjes 100 micrometer zijn. De eerste methode vindt een resultaat dat 10 keer zo groot is!

In dit verslag breiden we het model in de tweede methode uit. In dit uitgebreide model is de protoplanetaire schijf door twee verschillende deeltjes samengesteld. Deze deeltjes zijn 100 micrometer en 1 cm groot. Met dit model kunnen we zowel de intensiteit als de polarisatie verklaren. Dit model laat dus zien dat er wel degelijk mm of grotere deeltjes aanwezig kunnen zijn in tegenstelling tot wat de tweede methode eerst vond. We zijn er dus in geslaagd om de resultaten met elkaar overeen te laten komen.

Dit verslag gaat dieper op de materie in en laat de genomen tussenstappen zien om uiteindelijk tot deze conclusie te komen.

Abstract

Protoplanetary disks contain grains that form the basis of planet formation. These grains grow by lumping together. This happens until the growth-barrier is reached. Currently, there are two methods, based on (sub-) millimeter-wave observations, to obtain the size at which this growth-barrier is reached. One method is by measuring the spectral index and comparing this to calculated opacity values. This method showed grain sizes of mm or larger. The second method is through measuring the polarization and modeling protoplanetary disks to match this polarization result. This method however showed $\sim$100 μm sized grains. This paper reconciles this mismatch by expanding the model they used. First, we create our own basic Monte Carlo Radiative Transfer (MCRT) simulation code. This gives us a better understanding of the workings of a MCRT, which is then applied to a plane parallel atmosphere. Secondly, we use a dust model to see how the opacity and polarization depend on the maximum grain size. Thirdly, we combine the dust model and RADMC-3D, an advanced MCRT code, to create images of a disk model populated by 100 μm sized grains. Finally, we expand this disk model by populating an additional grain species of 1 cm-sized grains in the disk. This model is able to replicate the expected polarization and opacity values with a moderately thick disk with the presence of 1 cm grains as the opacity index method found and thus reconciling the mismatch. Therefore, we conclude that a further longer wavelength observation of disks would be crucial to determine the maximum grain radius in disks.
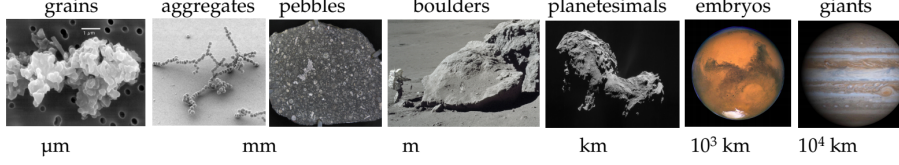
Contents

Figure 1: The growth stages grains undergo to form planets (Ormel, 2016).

1 Introduction

Planet formation starts in a protoplanetary disk. This protoplanetary disk is populated with gas and grains. These grains will lump together over time to create larger bodies. These steps are shown in Figure 1. However, during this process, the grains will reach a growth barrier. This growth barrier makes it harder for particles to grow to larger sizes.

There are currently two methods to measure the size of the grains and thus to measure at which size the growth barrier is reached. Both of these methods rely on (sub-)millimeter-wave observations.

The first method is by measuring the spectral index of an object. The spectral index represents how the emergent flux at about millimeter wavelengths depends on the wavelength at which the object is observed.

$$\alpha = \frac{\log_{10}(F_{\nu_1}/F_{\nu_2})}{\log_{10}(\nu_1/\nu_2)}, \tag{1}$$

where F_ν is the flux density, ν is the frequency and α is the spectral index.

Similarly, we can measure the frequency dependence of the absorption opacity of dust grains κ_{abs} such that

$$\beta = \frac{\log_{10}(\kappa_{\mathrm{abs},\nu_1}/\kappa_{\mathrm{abs},\nu_2})}{\log_{10}(\nu_1/\nu_2)}, \tag{2}$$

where β is the opacity index.

By looking at a homogeneous slab of dust grains we can obtain an expectation for the spectral index. The homogeneous slab of dust grains has a temperature T and the thickness has an optical depth of τ_ν, the emergent intensity from this slab can be expressed as

$$I_\nu(\tau_\nu) = I_\nu(\tau_\nu = 0)e^{-\tau_\nu} + B_\nu(T)(1 - e^{-\tau_\nu}), \tag{3}$$

where $I_\nu(\tau_\nu)$ is the intensity, $B_\nu(T)$ is the Planck function (Rybicki and Lightman, 1979). Suppose there is no background radiation ($I_\nu(\tau_\nu = 0) = 0$), and thus, we obtain

$$I_\nu(\tau_\nu) = B_\nu(T)(1 - e^{-\tau_\nu}). \tag{4}$$

If we adopt the Rayleigh-Jeans law for the Planck function, we expect $B_\nu(T) \propto \nu^2$. The optical depth is defined by $\tau_\nu = \Sigma_d \kappa_{\mathrm{abs}}$, where Σ_d is the
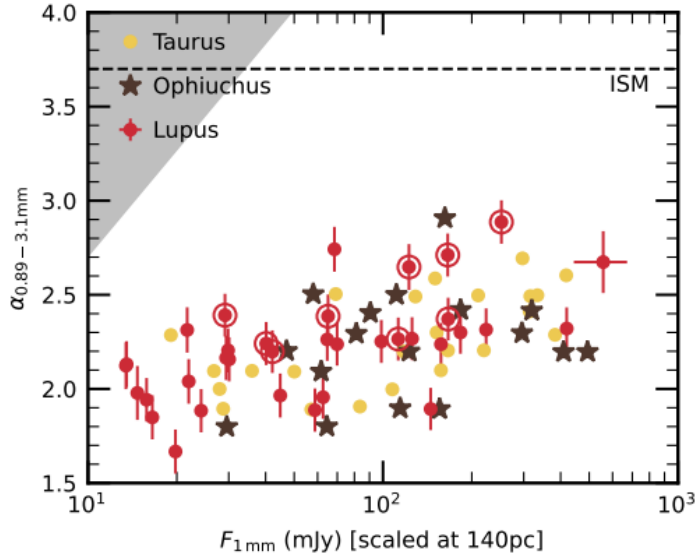
Figure 2: Spectral index measurements of different protoplanetary disks. These measurements were performed between 1 and 3 mm wavelengths. A mean spectral value of 2.23 ± 0.06 was found. (Tazzari et al., 2021)

surface density of dust grains. With these definitions, the above equation yields

$$\alpha \simeq 0 \qquad (\tau_\nu \gg 1), \tag{5}$$

$$\alpha \simeq \beta + 2 \quad (\tau_\nu \ll 1). \tag{6}$$

Since protoplanetary disks have been believed to be optically thin, measurements of the spectral index α can infer the optical index β of grains in the disk.

Figure 2 shows the measurements of the spectral index for various protoplanetary disks based on the Atacama Large Millimeter/submillimeter Array (ALMA) (Tazzari et al., 2021). A mean spectral value is 2.23 ± 0.06. Therefore, if we assume that disks are optically thin, the inferred opacity index is 0.23. Figure 3 shows how the opacity index β varies with the maximum grain radius in disks. From Figure 3, the opacity index of 0.23 is likely resulting from mm-sized or larger grains (see also Draine (2006)).

The second method is by measuring the polarization flux coming from protoplanetary objects. Several of these measurements are plotted in Figure 4. They measured a mean polarization value of $\sim 1\%$. With models of protoplanetary disks, they showed that maximum grain size should be constrained to 150 μm (Kataoka et al., 2016).

The target of this paper is to reconcile this mismatch between these two methods. Here we will look at expanding the model from Kataoka et al. (2015)
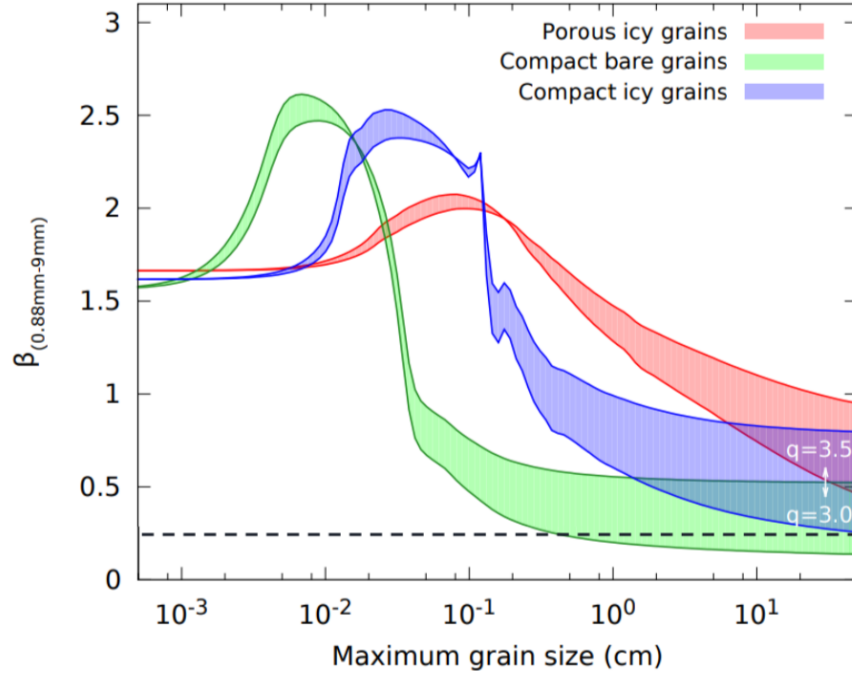
Figure 3: Opacity index calculations were performed for wavelengths between 0.88 and 9 mm (Testi et al., 2014). We can see how different grain compositions and sizes affect the opacity index. *Porous icy grains*: composed by astronomical silicates, carbonaceous material, and water ice, with relative abundance as in (Pollack et al., 1994) and a porosity of 50%. *Compact icy grains*: compact grains with the same composition as porous icy grains. *Compact bare grains*: same composition as the compact icy grains, but without the water ice. The horizontal line at 0.23 displays the mean opacity value obtained from Figure 2.
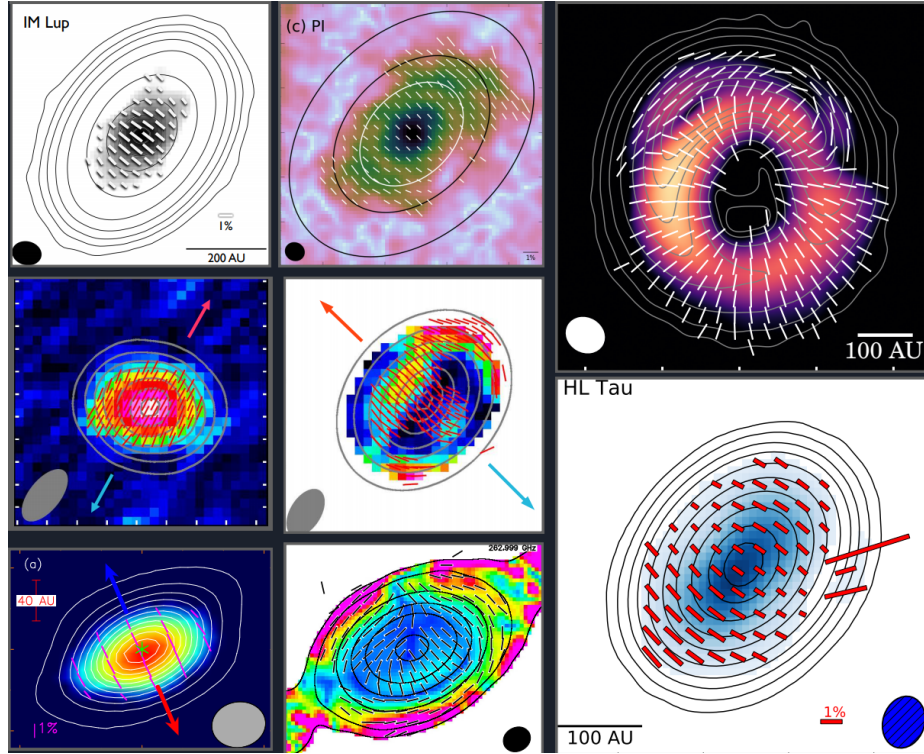
Figure 4: Several polarization measurements of different protoplanetary disks performed by the ALMA telescope. (Kataoka et al., 2016), (Stephens et al., 2017), (Hull et al., 2018), (Ohashi et al., 2018), (Bacciotti et al., 2018), (Girart et al., 2018), (Lee et al., 2018), (Dent et al., 2019). These disks typically show a polarization of ~1%.

by inserting a secondary grain population as opposed to the single grain population used before.

In section 2 we will look at numerical methods to simulate photon packages through a plane parallel atmosphere. This method is then compared to analytical solutions to the problem. In section 3 we build our dust model and two protoplanetary disk models, a single grain and a dual grain model. In section 4 we see how changes in the grain size affect the polarization. We also look at the spectral index and polarization for both protoplanetary disk models. We discuss the outcomes of the simulation results in section 5 and conclude in section 6.

2 Monte Carlo Radiative Transfer in Plane Parallel Atmosphere

We will look at a simple atmosphere to demonstrate the use of Monte Carlo Radiative Transfer (MCRT) simulation. Our atmosphere has a vertical optical depth of τ_{max} and is plane parallel to the ground. The optical depth, τ, is constant throughout the atmosphere. Photon packages propagate from the ground into the atmosphere and will experience scattering events. When a scattering event occurs a new direction of propagation will be determined. This process continues until either the photon escapes the atmosphere or is absorbed by the ground. This is displayed in Figure 5.

2.1 Analytical method

The radiative transfer equation for our setup is (Rybicki and Lightman, 1979)

$$\mu \frac{\partial I_\nu}{\partial \tau} = I_\nu - S_\nu, \tag{7}$$

$$S_\nu = \epsilon_\nu B_\nu + (1 - \epsilon_\nu) J_\nu, \tag{8}$$

where I_ν is the specific intensity, S_ν is the source function, B_ν is the Planck function, ϵ_ν is the photon destruction efficiency, and J_ν is the mean intensity. τ is the optical depth of the atmosphere along the vertical direction measured from top to bottom and $\mu \equiv \cos\theta$; where θ is the angle between the ray and the vertical direction. The mean intensity is defined by

$$J_\nu = \frac{1}{4\pi} \oint I_\nu d\Omega, \tag{9}$$

where Ω is the solid angle.

We are interested in solving this set of equations for I_ν. There are two famous analytical approaches to the problem: the Milne Eddington approximation and the Chandrasekhar solution.

To be able to solve this problem three assumptions are made:
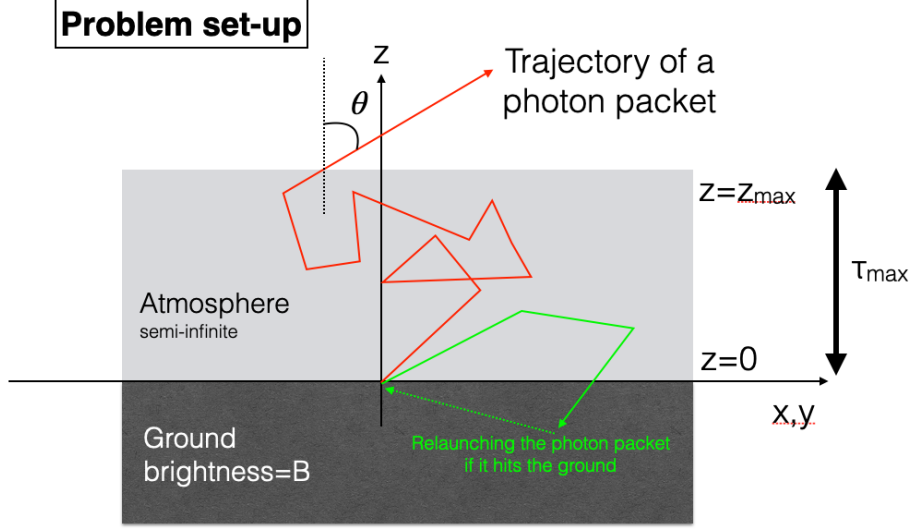
1. $S_\nu = B_\nu$

8

Figure 5: A schematic view of light scattering in a plane parallel atmosphere. A photon package is emitted from the origin in a random upwards direction. The photon package will scatter around until it either reaches the ground or until it escapes the atmosphere.

2. $\epsilon = 0$

3. isotropic scattering throughout the atmosphere.

2.1.1 Milne Eddington approximation

The Milne Eddington approximation solves the set of equations by invoking the radiation moments. These are defined as

$$H = \frac{1}{4\pi} \oint \mu I d\Omega, \tag{10}$$

$$K = \frac{1}{4\pi} \oint \mu^2 I d\Omega. \tag{11}$$

The third radiation moment is given by the *Eddington approximation*

$$J = 3K. \tag{12}$$

This approximation becomes especially good for an isotropic field.

Solving for the radiation moments as a function of the optical depth with

9

the radiative transfer equation yields

$$J(\tau) = 3H_0\left(\tau + \frac{2}{3}\right), \tag{13}$$

$$H(\tau) = H_0, \tag{14}$$

$$K(\tau) = H_0\left(\tau + \frac{2}{3}\right), \tag{15}$$

where H_0 is an integration constant related to the brightness of the ground.

With the use of the definition of the mean intensity and the two boundary conditions

$$I(\tau, \mu < 0) \to 0(\tau \to 0), \tag{16}$$

$$I(\tau, \mu > 0)e^{-\tau/\mu} \to 0(\tau \to \infty), \tag{17}$$

we obtain

$$I(\tau, \mu > 0) = 3H_0\left(\tau + \mu + \frac{2}{3}\right), \tag{18}$$

$$I(\tau, \mu < 0) = 3H_0\left(\tau + \mu + \frac{2}{3} - \left(\mu + \frac{2}{3}\right)e^{\tau/\mu}\right). \tag{19}$$

This simplifies at the top of the atmosphere ($\tau = 0$) to

$$I(\tau = 0, \mu > 0) = 3H_0\left(\mu + \frac{2}{3}\right). \tag{20}$$

2.1.2 Chandrasekhar solution

While the Milne Eddington solution is not exact, the Chandrasekhar solution is in fact exact. A useful polynomial fitting to the fourth-order is given by (Chandrasekhar, 1960; Peraiah, 1996)

$$\frac{I(0,\mu)}{H_0} = 3\left(\mu + 0.70692 - \frac{0.08392}{1 + 4.45808\mu} - \frac{0.03619}{1 + 1.59178\mu} - \frac{0.00946}{1 + 1.10319\mu}\right). \tag{21}$$

This equation would return the exact solution to our problem when the Chandrasekhar solution would be fit to the nth order with $n \to \infty$.

2.2 Numerical method: Monte Carlo radiative transfer

To test both of these solutions we use MCRT. MCRT is a numerical method that simulates photon packages coming from a light source. These photon packages are then traveling through an atmosphere or protoplanetary disk until a scattering event occurs. At this scattering event, a new direction is determined depending on the characteristics of the photon package and scattering medium.

2.2.1 Numerical procedures

Here we will describe the procedures to simulate light in a plane parallel atmosphere.

The first step is to determine the initial propagation of the package. This is achieved by generating two random variables, ε_1 and ε_2, in the range of 0 to 1. These random variables are then transformed into a θ and ϕ direction for the photon,

$$\cos\theta \equiv \mu = \sqrt{\varepsilon_1}, \tag{22}$$

$$\phi = 2\pi\varepsilon_2. \tag{23}$$

This distributes the photon uniformly in an upwards direction.

The next step is to determine the distance the photon travels until the next scattering event occurs. The number of photons decreases with $e^{-\tau}$. Thus we have

$$\tau = -\ln\varepsilon_3, \tag{24}$$

with ε_3 being a randomly generated variable in the range of 0 to 1. This corresponds with a distance of $s = \tau/\tau_{max}$. Thus the next scattering event occurs at:

$$x_1 = x_0 + s\sin\theta\cos\phi, \tag{25}$$

$$y_1 = y_0 + s\sin\theta\sin\phi, \tag{26}$$

$$z_1 = z_0 + s\cos\theta. \tag{27}$$

At the new position, we check if the photon has either escaped the atmosphere or is absorbed by the ground. If neither occurred, then the photon package will be isotropically scattered. Three new random variables, ε_1, ε_2, and ε_3, are generated. And then transformed to μ, ϕ, and τ according to:

$$\mu = 2\varepsilon_1 - 1, \tag{28}$$

$$\phi = 2\pi\varepsilon_2, \tag{29}$$

$$\tau = -\ln\varepsilon_3. \tag{30}$$

Again the photon is displaced according to equations 25, 26 and 27. This repeats itself until the photon escapes the atmosphere or when the photon is absorbed by the ground.

2.3 Comparison of MCRT with analytical solutions

By simulating a large number of photons we can approach the exact values for the intensity and radiation moments. We can then compare these to the analytical solutions.
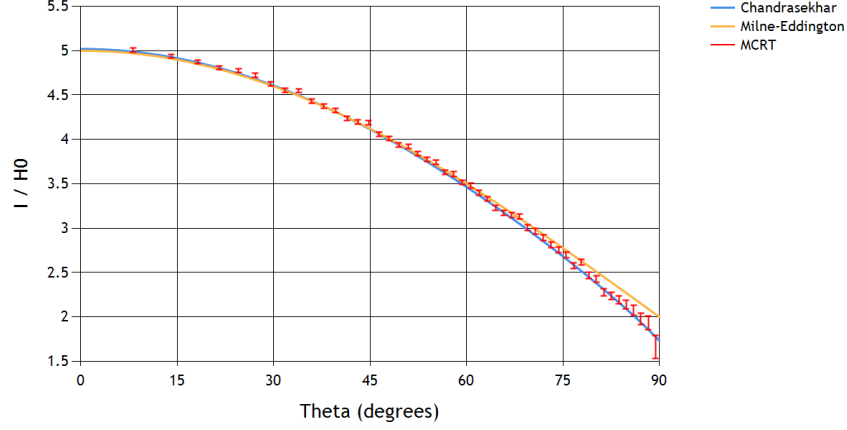
Figure 6: The emergent intensity plotted verses the emergent angle of the photons once it has escaped the plain parallel atmosphere. The results of the MCRT are compared to the Milne-Eddington approximation and the Chandrasekhar solution(equations 20 and 21, respectively).

2.3.1 Emergent intensities

We obtain the emergent intensity for each angle, by counting how many photon packages escape the atmosphere for each angle. We compare this with equations 20 and 21, as shown in Figure 6. At high θ values we can see that the Chandrasekhar solution and the Milne-Eddington approximation diverge. This is because at the top of the atmosphere the radiation field becomes anisotropic so that the Eddington approximation (Equation 12) is no longer valid. This results in the difference between the two solutions. We also see that the results from the MCRT match with the more exact Chandrasekhar solution.

2.3.2 Radiation moments

The MCRT is not only able to obtain the emergent intensities, but also the radiation moments throughout the atmosphere. We compare this with the radiation moments obtained from the Milne-Eddington approximation (Equation 13). This comparison is plotted in Figure 7. We can see that the MCRT results for the mean intensity deviate from the approximate mean intensity at both the top and bottom of the atmosphere. This is due to the anisotropic radiation field at these places and thus the Milne-Eddington approximation breaks down.
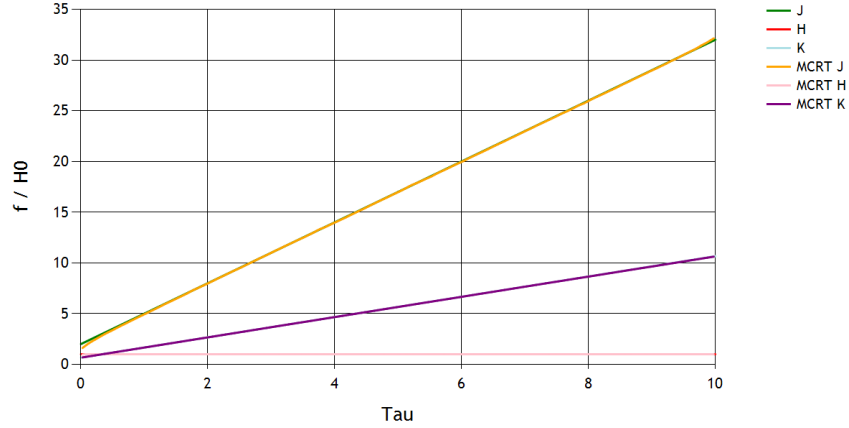
12

Figure 7: The different radiation moments obtained from the Milne-Eddington approximation compared with the MCRT results throughout the atmosphere. We see that the mean intensity results slightly deviates from the Milne-Eddington approximation at the top and bottom atmosphere. This is because there is an anisotropic radiation field at these regions.

3 Simulation setups for millimeter-wave polarization of protoplanetary disks

This section will provide the different models used for the protoplanetary disk. We will describe the dust model used. This dust model will be used for two protoplanetary disks. One with a single grain population and the other with two grain populations.

3.1 Dust models

The first step at a more complex system is to introduce dust particles that do not create isotropic scattering. We assume the same dust composition as Kataoka et al. (2015). It uses a mass fraction with silicate $= 0.225$, organics $= 0.301$, water-ice $= 0.474$, and a porosity of 0.25. The size distribution of the dust grains is set to $n(a) \propto a^{-3.5}$, with a being the size of the grains. The minimum dust size is taken to be 0.01 μm, with a varying maximum size. With the use of mie theory (Mie, 1908; Bohren and Huffman, 1983), the absorption and scattering coefficients and scattering matrix are calculated. This is done with the program OpTool (Dominik et al., 2021).

3.2 Disk models

3.2.1 Single grain model

We adopt the same disk and dust models as Kataoka et al. (2015) to simulate millimeter-wave scattering polarization of a disk. This dust is distributed according to the density function:

$$\rho_d = \Sigma_0 \exp\left[-\frac{1}{2}\left(\frac{r-r_d}{w_d}\right)^2\right] \frac{1}{\sqrt{2\pi}h_g} \exp\left[-\frac{1}{2}\left(\frac{z}{h_g}\right)^2\right], \qquad (31)$$

where $\Sigma_0 = 0.6 \text{ g cm}^{-2}$, $r_d = 173$ AU, $w_d = 27$ AU, and $h_g = 19.8$ AU $(r/r_d)^{1.5}$. The total mass of the disk then $5 \cdot 10^{-3} M_\odot$. The central star at the center of the disk is taken to be 1.9 $M_\odot$. The density is set to 0, when $r > 70$ AU or $r < 300$ AU.

3.2.2 Dual grain model

The dual population model has two grain species as opposed to the single grain species from the previous section. One grain population has a maximum size of 100 μm, while the second population has a maximum size of 1 cm. Larger-sized grain would have fallen into the midplane and therefore the disk height of the larger-sized particles is lower. A schematic view of the cross-section of the protoplanetary disk is drawn in Figure 8.

The same density function, equation 31, is used with two changes in parameters, the height and surface density. The height ratio of the two populations is assumed to be $h_g^L = 0.1h_g^S$, with $h_g^S = 19.8$ AU $(r/r_d)^{1.5}$. A schematic view is shown in Figure 8.

In the dual grain model, there are two free parameters. One is the mass ratio between small and large grains, and the other one is the optical depth of the disk.

3.3 MCRT simulations

We use RADMC-3D (Dullemond et al., 2012) to perform radiative transfer simulations of the disks. A simulation with RADMC-3D consists of two parts: thermal and scattering Monte Carlo simulations.

In this study, we assume a fixed temperature of T=38.66 K instead of performing the thermal Monte Carlo simulations. This temperature is the temperature at the midplane at the center disk of the temperature estimation used by Kataoka et al. (2015). This is done since it removes the need to simulate the temperature of the disk and thus increases the speed at which the disk can be simulated. This is possible since no significant changes in the results were found between the fixed temperature and a simulated temperature.

For the scattering Monte Carlo part, we assume a photon packet of $N = 2 \cdot 10^7$ considering the full Stokes parameters. The Stokes parameters are four values that describe the intensity and polarization of the light. These four
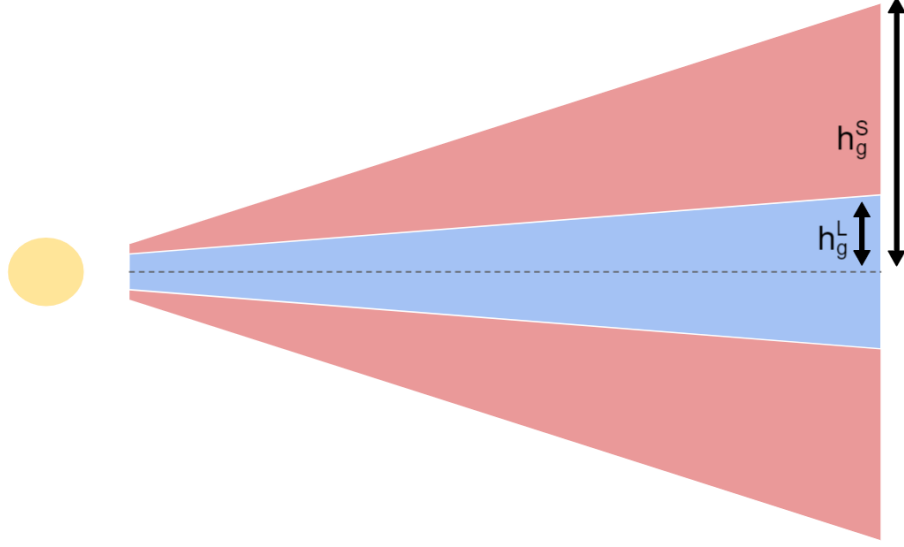
Figure 8: A schematic side view of the dual proposed protoplanetary disk setup. The disk is populated by two grain populations with a maximum size of 100 μm and 1 cm. The red area represents the height of the disk for the smaller particles, while the blue area represents the area for the larger particles.

values are the intensity, I, horizontal polarization, Q, diagonal polarization, U, and circular polarization, V. The linear polarization fraction is given by $P = \sqrt{Q^2 + U^2}/I$.

4   Results

This section will provide the results of our paper. We will look at how different grain sizes have a different effect on the opacity's and polarization. Then we look at how the grain size has an effect on the single grain model and at last we look for which parameters the dual grain model is able to reproduce the expected spectral and polarization values.

4.1   Grain size effect on opacity's and polarization

Changes in the maximum grain size result in different values for the absorption and scattering coefficients. Two different maximum grain sizes, 1 and 100 μm are shown in Figure 9. The scattering coefficient for 1 μm drops off massively, relative to its absorption coefficient when the wavelength of light starts to approach the millimeter regime. This is opposed to the 100 μm grain size, where the scattering coefficients are comparable to the absorption coefficients into the mm regime.
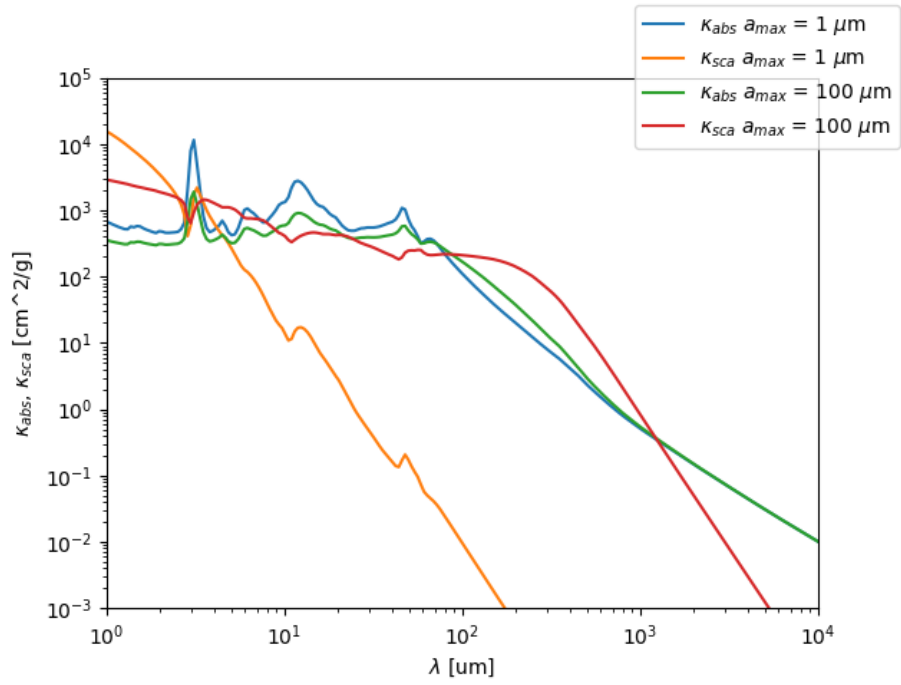
Figure 9: Scattering and absorption coefficients calculated at different wavelength light for both 1 and 100 μm grain sizes. The scattering coefficient for 1 μm grains is much less when looking at > 10 μm wavelength light.
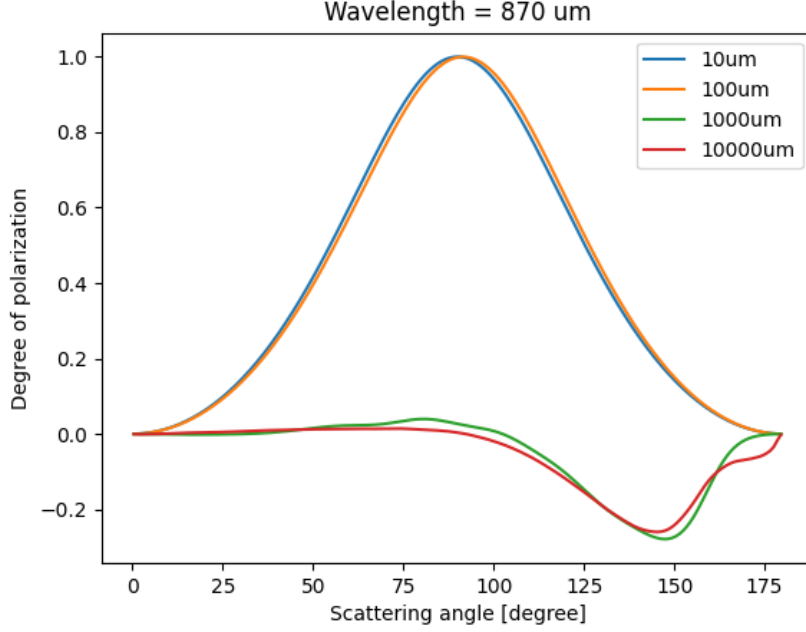
Figure 10: The degree of polarization created when a scatter event occurs with a particular angle. This is plotted for several grain sizes: 10 μm, 100 μm, 1 mm and 1 cm. The polarization reaches unity when $2\pi a/\lambda < 1$. This is due to Rayleigh scattering.

Another effect of grain sizes is found in the created polarization. In Figure 10 is the polarization as a function of the scatter angle plotted for various size distributions. It shows that the polarization reaches unity for the smaller maximum grain sizes and peaks at $\theta = 90$ degrees. This is due to Rayleigh scattering.

These two phenomena have two opposing effects. First of all, larger grain sizes have higher scattering coefficients as seen in Figure 9. Secondly, the polarization after a single scattering event is greater for smaller grain sizes. These two effects are plotted in Figure 11 for 870 μm wavelength light. Here $\omega = \kappa_{sca}/(\kappa_{sca} + \kappa_{abs})$ is the single scattering albedo and $p = -Z_{12}/Z_{11}$ the polarization at 90 degrees. As a_{max} becomes larger than $\lambda/2\pi$ the polarization drops to zero, while the albedo goes to unity. The combination of the two effects, $p\omega$, gives a function from which we can obtain at which grain size contributes the most to polarization.
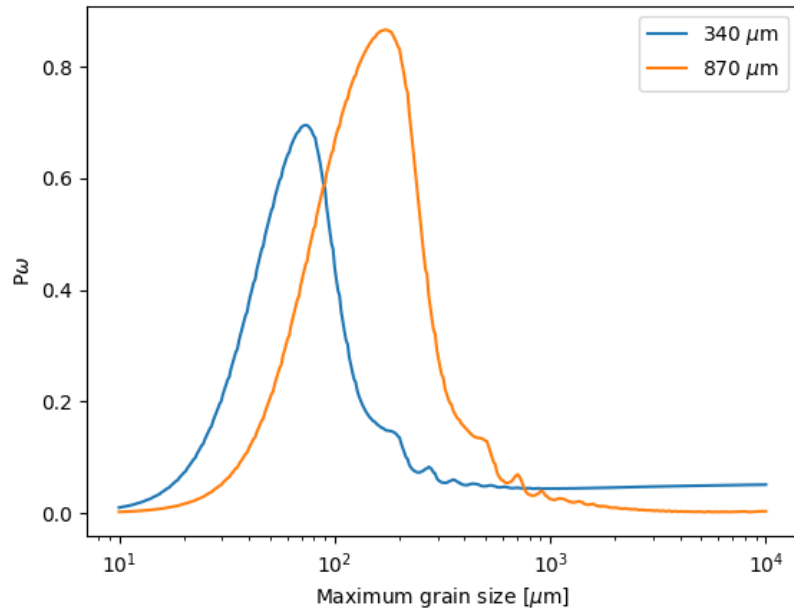
Figure 11: The effectiveness of creating polarization light as a function of the maximum grain size. With $\omega = \kappa_{sca}/(\kappa_{sca} + \kappa_{abs})$ and $p = -Z_{12}/Z_{11}$ the polarization at 90 degrees.
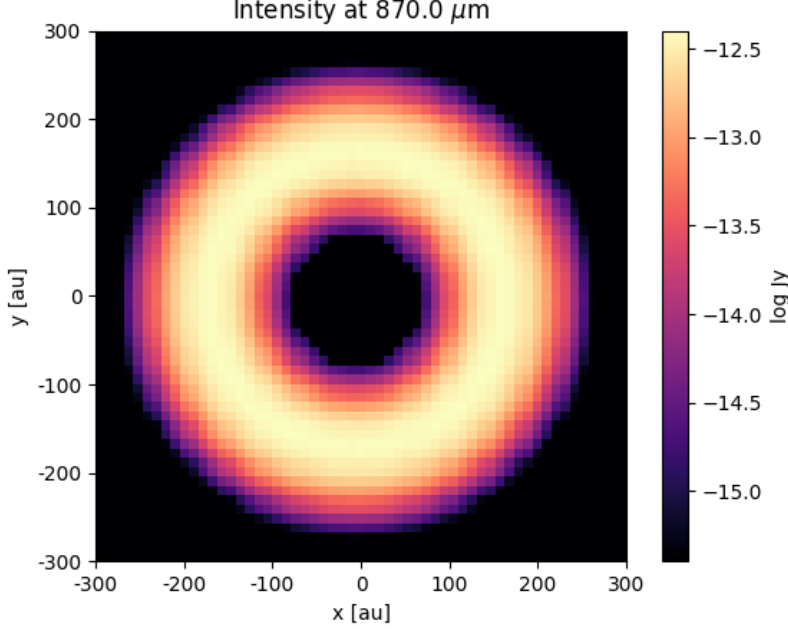
Figure 12: An example plot of the intensity for the single grain protoplanetary disk model. This example shows a disk with a maximum grain size of 100 μm, observed at 870 μm.

4.2   Single grain protoplanetary disk model

Figures 12 and 13 show the images of total intensity and polarization fraction obtained by RADMC-3D, respectively. The bars in Figure 13 represent the angle of the linear polarization and is calculated through $\theta = 0.5 \arctan(U/Q)$. Close to the star the polarization is parallel to the radial direction. At a certain distance the polarization flips 90 degrees.

This phenomenon can be explained when we look at the surrounding radiation. As shown in Figure 10, dust grains tend to make the scattered light polarized perpendicular to the direction of the incident light. The polarization pattern shown in Figure 13 is best explained with the help of Figure 14 (Kataoka et al., 2015).

At (A) most of the radiation is coming from the x-direction. Thus most of the polarization is created at a 90 degree angle, which results in polarization in the y-direction. For (B) most of the radiation is in the y-direction, and thus the resulting polarization is in the x-direction. Somewhere between (A) and (B) these effects are equal to each other. This results in zero polarization, which can also be seen in Figure 13 at $\sim$200 AU away from the star.

In Figure 15 is shown how the mean polarization of the disk changes as
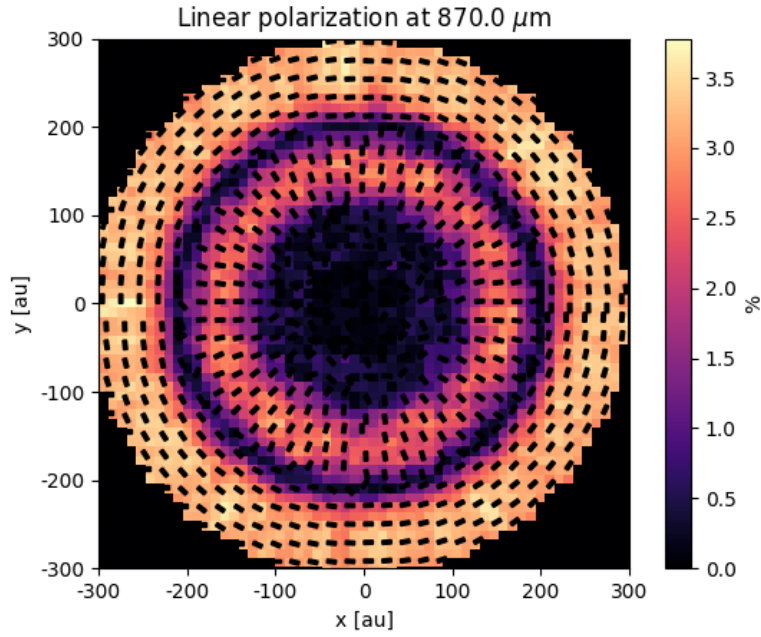
Figure 13: An example plot of the polarization for the single grain protoplanetary disk model. This example shows a disk with a maximum grain size of 100 μm, observed at 870 μm. The black bars represent the polarization angle and are calculated through: $P = \sqrt{Q^2 + U^2}/I$. The flip of polarization is explained in Figure 14.
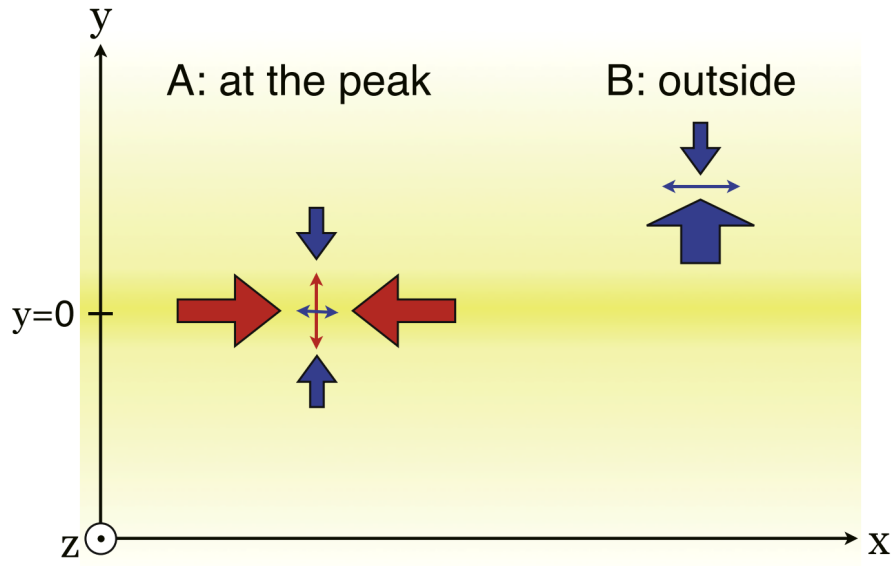
Figure 14: Explanation of the creation of polarized light. (Kataoka et al., 2015) At (A) most of the radiation is coming from the x-direction. This creates polarization in the y-direction since most of the polarization is created at a 90 degree angle. For (B) most of the radiation is in the y-direction, and thus the resulting polarization is in the x-direction. Somewhere between (A) and (B) these effects are equal to each other. This results in zero polarization.
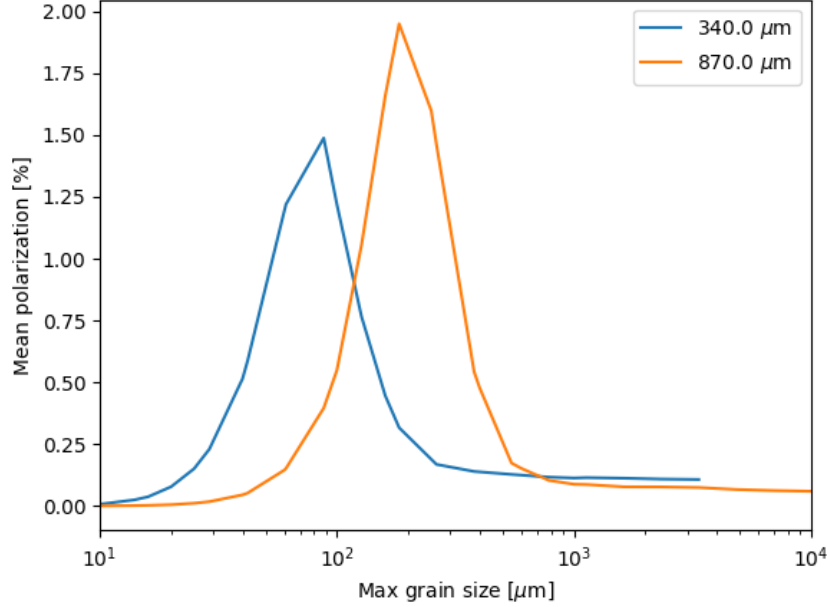
Figure 15: The mean polarization measured for the simple protoplanetary disk model as a function of the maximum grain size. The observed grain size dependence can be understood by $P\omega$ of grains, as shown in Figure 11.

a function of the maximum grain size. These results can be understood by comparing them to $P\omega$ grains, as shown in Figure 11.

4.3   Dual grain protoplanetary disk model

We consider two parameters for our dual grain model, the mass fraction ξ and the optical depth τ.

The mass fraction is defined as,

$$\xi \equiv \frac{\Sigma_L}{\Sigma_L + \Sigma_S},$$

(32)

and thus all mass is in the smaller sized particles when $\xi = 0$, while all the mass is in the larger sized particles when $\xi = 1$. The optical depth is defined as,

$$\tau = \Sigma_S \kappa_S(\lambda) + \Sigma_L \kappa_L(\lambda),$$

(33)

where κ_S and κ_L are the absorption coefficients at wavelengths of λ. With these parameters, the spectral index and polarization are calculated. The polarization is then sampled at the center disk, at 173 AU away from the star, as shown in
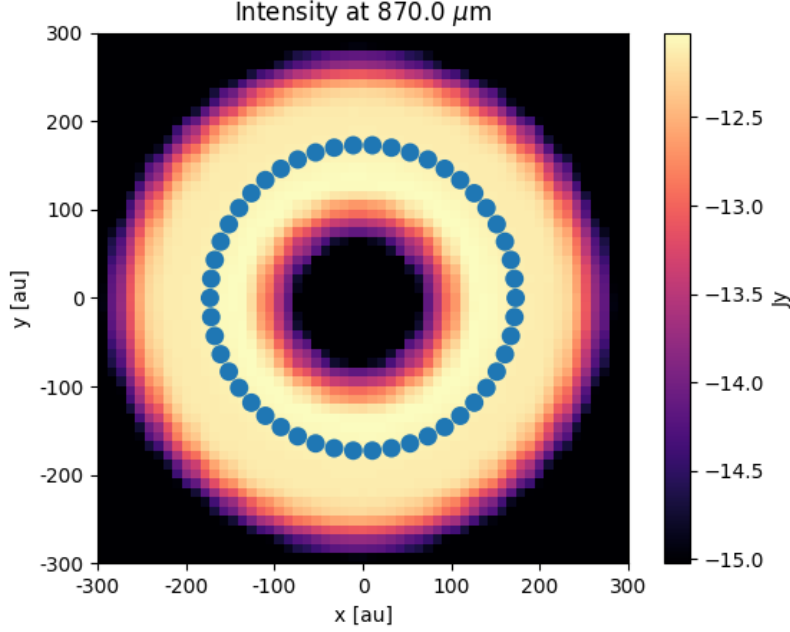
Figure 16: Illustration of the positions at which the polarization was sampled from the protoplanetary disk.

Figure 16. This is done since the optical depth of the disk is at this point equal to the optical depth parameter. The results are shown in Figures 17, 18 and 19.

As anticipated in equations 5 and 6, Figure 17 shows that the spectral index α decreases as τ increases. We also find that the mass ratio does not significantly affect spectral indices.

Figure 18 shows the polarization fractions of the dual grain model. At $\tau = 0.3$, a polarization fraction decreases as a fraction of the large grains increases. However, at $\tau = 10$, the mass ratio does not significantly affect polarization fractions except for the case of $\xi = 1$. This is because for an optically thick disk, small grains populated at the disk surface can create a 1% level polarization fraction due to scattering."

In Figure 19, we combine the results shown in Figures 17 and 18. The results are then compared with the observationally expected values. As a result, we conclude that mass fractions between 0.25 and 0.5 with an optical depth between 1 and 3 results in the expected values. Thus we are able to show that the polarization values can indeed be explained by 1 cm sized grains as opposed to the 150 μm as long as disks are moderately optically thick.
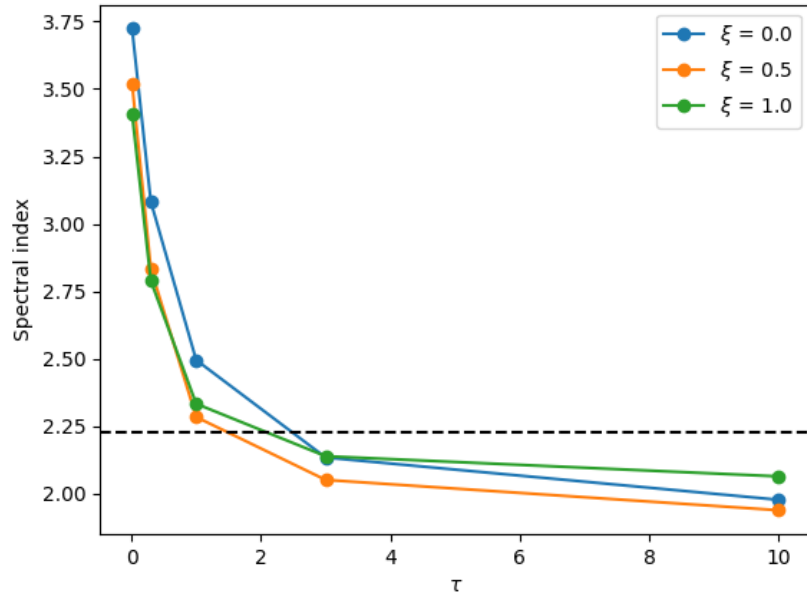
Figure 17: The calculated spectral values as a function of the optical depth. At low optical depths the spectral values matches with $\beta + 2$ from the dust model. The horizontal dashed line indicates the expected mean spectral index of ~ 2.23. These results indicate that observed protoplanetary disks are likely to have an optical depth of about 1 to 3.
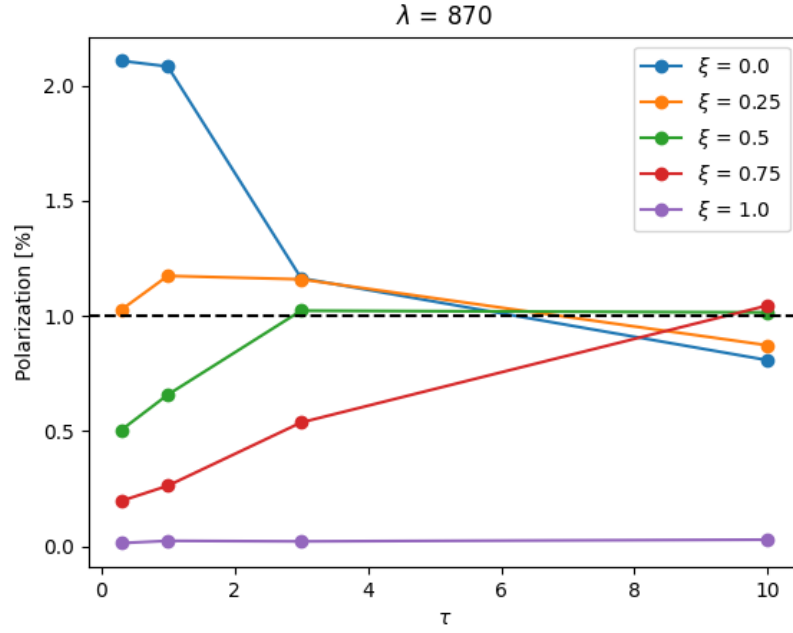
Figure 18: The calculated polarization values at the center of the disk as a function of the optical depth. When looking at the low optical depths, we see that the polarization is higher for the smaller sized particles as was expected. We see that the polarization converges to one value at higher optical depths, except for the case of $\xi = 1$. Comparing the results to the expected $\sim 1\%$, we note that this can be obtained by either having a optically thin disk with a mass fraction between 0.25 and 0.5 or for a optically thick disk with a non uniform mass fraction.
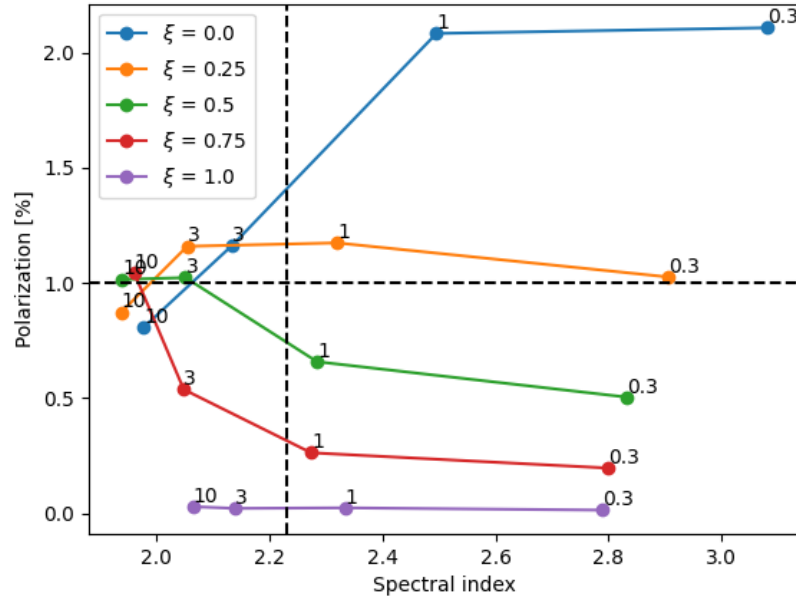
Figure 19: Combination of the results in Figures 17 and 18. The numbers at each data point represent the optical depth. The horizontal dashed line is the expected polarization of ∼1%. The vertical dashed line is the expected spectral index of ∼2.23. This result shows that a protoplanetary disk should be moderately thick with an optical depth between 1 and 3. And has a mass fraction between 0.25 and 0.5.

5 Implications for grain radius in protoplanetary disks

Our results imply that a polarization fraction around $\sim$1% with low values of the spectral index is most likely resulting from a moderately optically thick disk. In this case, scattering polarization is arising from 100 μm size grains at the disk surface. It is possible that further large grains are hidden in the thin midplane layer. Therefore, to reveal the grain radius at the disk midplane, further longer wavelength observations, cm-wave, would be crucial because disks are likely optically thin at such a longer wavelength.

6 Conclusion

In this study, we have performed Monte Carlo radiative transfer simulations to investigate millimeter-wave polarization of protoplanetary disks. As a result, we have shown that a dual grain populated protoplanetary disk with 100 μm and 1 cm sized grains is able to both explain the $\sim$1% polarization and the 2.23 spectral index value. This is possible for a moderately, $1 < \tau < 3$, thick disk. With this conclusion, we were able to reconcile the mismatch between the previously determined grain sizes.

Further observations at cm-wave wavelengths would be essential to find larger-sized grains. At these wavelengths, the disk would likely be optically thin.

References

Bacciotti, F., Girart, J. M., Padovani, M., Podio, L., Paladino, R., Testi, L., Bianchi, E., Galli, D., Codella, C., Coffey, D., Favre, C., and Fedele, D.: 2018, *The Astrophysical Journal Letters* **865(2)**, L12

Bohren, C. F. and Huffman, D. R.: 1983, *Absorption and scattering of light by small particles*

Chandrasekhar, S.: 1960, *Radiative transfer*, Dover publications

Dent, W. R. F., Pinte, C., Cortes, P. C., Ménard, F., Hales, A., Fomalont, E., and de Gregorio-Monsalvo, I.: 2019, *Monthly Notices of the Royal Astronomical Society* **482(1)**, L29

Dominik, C., Min, M., and Tazaki, R.: 2021, *OpTool: Command-line driven tool for creating complex dust opacities*, https://github.com/cdominik/optool

Draine, B. T.: 2006, *The Astrophysical Journal* **636(2)**, 1114

Dullemond, C. P., Juhasz, A., Pohl, A., Sereshti, F., Shetty, R., Peters, T., Commercon, B., and Flock, M.: 2012, *RADMC-3D: A multi-purpose radiative transfer tool*

Girart, J. M., Fernández-López, M., Li, Z. Y., Yang, H., Estalella, R., Anglada, G., Áñez-López, N., Busquet, G., Carrasco-González, C., Curiel, S., Galvan-Madrid, R., Gómez, J. F., de Gregorio-Monsalvo, I., Jiménez-Serra, I., Krasnopolsky, R., Martí, J., Osorio, M., Padovani, M., Rao, R., Rodríguez, L. F., and Torrelles, J. M.: 2018, *The Astrophysical Journal Letters* **856(2)**, L27

Hull, C. L. H., Yang, H., Li, Z.-Y., Kataoka, A., Stephens, I. W., Andrews, S., Bai, X., Cleeves, L. I., Hughes, A. M., Looney, L., Pérez, L. M., and Wilner, D.: 2018, *The Astrophysical Journal* **860(1)**, 82

Kataoka, A., Muto, T., Momose, M., Tsukagoshi, T., Fukagawa, M., Shibai, H., Hanawa, T., Murakawa, K., and Dullemond, C. P.: 2015, *The Astrophysical Journal* **809(1)**, 78

Kataoka, A., Tsukagoshi, T., Momose, M., Nagai, H., Muto, T., Dullemond, C. P., Pohl, A., Fukagawa, M., Shibai, H., Hanawa, T., and Murakawa, K.: 2016, *The Astrophysical Journal* **831(2)**, L12

Lee, C.-F., Li, Z.-Y., Ching, T.-C., Lai, S.-P., and Yang, H.: 2018, *The Astrophysical Journal* **854(1)**, 56

Mie, G.: 1908, *Annalen der Physik* **330(3)**, 377

Ohashi, S., Kataoka, A., Nagai, H., Momose, M., Muto, T., Hanawa, T., Fukagawa, M., Tsukagoshi, T., Murakawa, K., and Shibai, H.: 2018, *The Astrophysical Journal* **864(1)**, 81

Ormel, C.: 2016, *Lecture notes in Planet formation*, `https://staff.fnwi.uva.nl/c.w.ormel/Teaching/planet-formation.pdf`

Peraiah, A.: 1996, *Bulletin of the Astronomical Society of India* **24**, 397

Pollack, J. B., Hollenbach, D., Beckwith, S., Simonelli, D. P., Roush, T., and Fong, W.: 1994, *The Astrophysical Journal* **421**, 615

Rybicki, G. B. and Lightman, A. P.: 1979, *Radiative processes in astrophysics*

Stephens, I. W., Yang, H., Li, Z.-Y., Looney, L. W., Kataoka, A., Kwon, W., Fernández-López, M., Hull, C. L. H., Hughes, M., Segura-Cox, D., Mundy, L., Crutcher, R., and Rao, R.: 2017, *The Astrophysical Journal* **851(1)**, 55

Tazzari, M., Testi, L., Natta, A., Williams, J. P., Ansdell, M., Carpenter, J. M., Facchini, S., Guidi, G., Hogherheijde, M., Manara, C. F., Miotello, A., and van der Marel, N.: 2021, *The first ALMA survey of protoplanetary discs at 3 mm: demographics of grain growth in the Lupus region*

Testi, L., Birnstiel, T., Ricci, L., Andrews, S., Blum, J., Carpenter, J., Dominik, C., Isella, A., Natta, A., Williams, J. P., and Wilner, D. J.: 2014, in H. Beuther, R. S. Klessen, C. P. Dullemond, and T. Henning (eds.), *Protostars and Planets VI*, p. 339